Applied Physics Letters

Role of local chemical fluctuations in the melting of medium entropy alloy CoCrNi

Cite as: Appl. Phys. Lett. **119**, 121904 (2021); https://doi.org/10.1063/5.0064299
Submitted: 22 July 2021 . Accepted: 08 September 2021 . Published Online: 22 September 2021

Wu-Rong Jian, Liang Wang, Wenbo Bi, Shuozhi Xu, Irene J. Beyerlein, et al.

Applied Physics Letters ARTICLE scitation.org/journal/apl

Role of local chemical fluctuations in the melting of medium entropy alloy CoCrNi

Cite as: Appl. Phys. Lett. **119**, 121904 (2021); doi: 10.1063/5.0064299
Submitted: 22 July 2021 · Accepted: 8 September 2021 ·
Published Online: 22 September 2021

Wu-Rong Jian,[1,a)] Liang Wang,[2] Wenbo Bi,[2] Shuozhi Xu,[1] and Irene J. Beyerlein[1,3]

AFFILIATIONS

[1]Department of Mechanical Engineering, University of California, Santa Barbara, California 93106-5070, USA
[2]College of Science, Hunan Agriculture University, Changsha, Hunan 410128, People's Republic of China
[3]Materials Department, University of California, Santa Barbara, California 93106-5050, USA

Note: This paper is part of the APL Special Collection on Metastable High Entropy Alloys.
[a)]**Author to whom correspondence should be addressed:** wurong@ucsb.edu

ABSTRACT

Medium- to high-entropy alloys are characterized by fluctuations in chemical composition, i.e., lattice distortion (LD) and chemical short-range ordering (CSRO). However, their roles in the melting of these alloys are still unclear. Using a combination of molecular dynamics and x-ray diffraction simulations, we investigate the effects of LD and CSRO on the melting of single crystalline CoCrNi, a medium entropy alloy (MEA). LD accelerates the melting process and reduces the melting temperature by lowering the energy barrier of the nucleation of amorphous clusters and then promoting the formation of amorphization. By contrast, CSRO divides CoCrNi MEA into CoCr clusters and Ni segregated regions, localizing LD to the CoCr regions and the boundaries between CoCr clusters and Ni regions. Such a LD localization reduces the area for the nucleation of the amorphous clusters in the ordered MEA at the start of melting, resulting in a lower free energy and, thus, a much higher melting temperature than the random MEA without CSRO. As the temperature rises in the ordered MEA, the degree of CSRO decreases slightly in the beginning and then experiences a rapid reduction in the last stage of melting.

Medium- and high-entropy alloys, collectively called multi-principal element alloys (MPEAs), are of fundamental and technological interest for their excellent mechanical properties,[1–4] e.g., high strength, high fracture toughness, and good ductility.[5] To realize mass production at low cost and high efficiency, additive manufacturing by selective laser melting has been recently utilized to fabricate MPEAs.[6–9] To further improve this technique, it is necessary to uncover the physical process of the melting of MPEAs. Research in this area, however, has not been intensely carried out.

Compared to conventional alloys consisting of one dominant element, MPEAs consist of multiple dominant elements, which give rise to significant chemical fluctuations. Consequences lead to lattice distortion (LD) and chemical short-range order (CSRO).[10,11] LD stems from the size differences in atomic species,[12,13] while CSRO forms after the long anneal of the solid solution alloys at relatively low temperatures.[14–16] These two structural characteristics in MPEAs contribute to superior resistance to dislocation motion[17,18] and promotion of nano-twinning.[19] These same fluctuations could affect the melting process of MPEAs. To date, the effects of LD and CSRO on the melting of MPEAs remain unexplored and direct observation of the structural evolution during melting at the nanoscale via *in situ* microscopy remains a challenge.

The melting process initiates over nanosecond and nanometer scales,[20,21] making molecular dynamics (MD) simulation a powerful tool to study the role of local chemical fluctuations in the structural evolution of MPEAs and related physical processes. In the past twenty years, MD simulations have been employed to study melting in a variety of metals, such as Cu,[20,22,23] Mg,[24] V,[25] and Na.[26] More recently, MD simulations have been combined with x-ray diffraction (XRD) simulation,[27] enabling mapping of the XRD pattern with the simulated atomic structure. In this way, *in situ* XRD experimental data can be interpreted with respect to spatial changes in the material. Recently, MD and XRD were joined to study shock-induced melting in a metallic glass[28] and Cu.[29] To date, this combination has not been applied to study melting in complex concentrated alloys, such as MPEAs.

In this work, we apply MD and XRD simulations to study the effects of LD and CSRO on the melting of CoCrNi, a medium entropy alloy (MEA). We demonstrate that the characteristics of LD, CSRO, and the solid–liquid transition are reflected in the x-ray patterns in reciprocal space. We show that LD leads to higher volumetric stress

and more significant stress fluctuations, promoting lattice instability, amorphization, and melting, and finally resulting in a lower melting temperature. CSRO divides CoCrNi MEA into CoCr clusters and Ni-rich regions. In this way, the amorphous clusters prefer to nucleate within the CoCr regions and at the boundaries of CoCr clusters and Ni regions, since CSRO localizes LD to these regions. As temperature increases, the CSRO begins to decompose but the reduction in the degree of CSRO is remarkably slight in the beginning, suggesting thermal stability. It only begins to disappear rapidly when the temperature exceeds 95% of the melting temperature.

We utilize LAMMPS[30] to conduct the MD simulations. The atomic interactions among the Co, Cr, and Ni atoms are described by the embedded-atom-method (EAM) interatomic potential developed by Li *et al.*[18] An average-atom (*A*-atom) EAM potential, which is a mean-field approximation of the atomic interactions in CoCrNi MEA, was developed in a prior work[19] and can be downloaded from https://github.com/wrj2018/Acta_2020.

First, we build the single crystalline *A*-atom sample with its $[1\bar{1}0]$, $[11\bar{2}]$, and [111] directions aligned with the *x*-, *y*-, and *z*-axes, respectively. The atomic model contains 1.84 million atoms and has the dimensions of $\sim 27 \times 27 \times 27\ \mathrm{nm}^3$. With the similar dimensions to the *A*-atom sample, a CoCrNi MEA with random atomic distribution, i.e., random MEA, and a CoCrNi MEA with CSRO, i.e., ordered MEA, are constructed. The details about the construction of MEA models are found in a prior paper[19] and the supplementary material. Figures 1(a)–1(c) display the atomic configurations for the *A*-atom sample, random, and ordered CoCrNi samples, respectively.

Next, the time step is set to 1 fs and all three samples are heated from 0 to 2000 K with the temperature increments of 20 K. After each temperature increment, the samples are equilibrated for 50 ps under isothermal-isobaric (NPT) ensemble with all stress components being zero. During the equilibrium, the volume, diffusion coefficient, amorphous atom percent, and CSRO parameters are obtained. The diffusion coefficient is calculated by

$$D = \lim_{t\to\infty} \frac{1}{6}\frac{\delta}{\delta t}\langle|\mathbf{r}(t+t_0) - \mathbf{r}(t_0)|^2\rangle, \tag{1}$$

where t is time and $\mathbf{r}$ is atomic position.[28] The CSRO is quantified by Warren–Cowley SRO parameters,[31,32] i.e., the positive α_{NiNi} and the negative α_{CoCr} for CoCrNi MEA. The absolute values of α_{NiNi} and α_{CoCr} are positively associated with the CSRO degree. At 0 K, LD can be estimated by the full width at half maximum (FWHM) of the radial distribution functions $g(r)$ and larger FWHM indicates higher degree of LD (see the supplementary material). Here, *A*-atom sample, containing no LD or CSRO, is regarded as a mean-field model of CoCrNi MEA. In random MEA, there is no CSRO while LD exists everywhere; in ordered MEA, CSRO is characterized by the CoCr clusters and the Ni-rich regions, and LD only exists within CoCr regions and at the boundaries between CoCr clusters and Ni regions. According to Table S2 in the supplementary material, the degrees of LD in random and ordered MEAs, represented by FWHM, are nearly the same but both are significantly larger than that of the *A*-atom sample. Thus, comparing the random MEA to the *A*-atom sample and the ordered MEA helps to elucidate the roles of LD and CSRO, respectively. The amorphous atoms are recognized by the polyhedral template matching method[33] implemented in OVITO[34] and referred to as "other" type atoms in this method. The XRD simulation is also applied (see the supplementary material).

To determine the MPEA effect on the moment of melting, we analyzed the variation in material volume with temperature. Figure 2(a) shows the volume–temperature curves for the three different MPEA samples. The sample volume increases as the temperature rises and, at a particular temperature, experiences a sharp jump, expanding by 3%–4%. Afterward, the volume resumes rising at a constant rate. For all materials, the volume jump occurs within a 20 K increment. Such a jump in volume is related to the solid–liquid transition and is commonly seen in studies of pure metals, such as Cu[20] and V.[35] Before the rapid expansion, the random CoCrNi MEA expands the fastest, followed by the ordered MEA and finally the *A*-atom sample with the lowest rate. After the jump, however, all these samples expand at nearly the same rate. The temperature at which the jump starts, point 1 (see Fig. 2) also depends on the material. The random MEA has the lowest point 1 temperature of 1680 K, followed by the ordered MEA with 1800 K, and the *A*-atom sample with 1820 K. The comparison between random MEA and *A*-atom sample shows that LD lowers the transition temperature. Between two MEAs, the higher the CSRO degree, the higher the temperature for the transition.

To establish the melting temperature for these MPEAs, we study the corresponding diffusion coefficient-temperature curves, which are presented in Fig. 2(b). For a given sample, a jump in the diffusion coefficient *D* by two orders of magnitude occurs at the same temperature as the jump in volume. In all sample types, *D* at point 2, where the jump completes, is 4000–6000 $\mu\mathrm{m}^2/\mathrm{s}$. The sudden change in *D* suggests the phase transition. The diffusion coefficients for liquids are several orders of magnitude larger than those for solids. The diffusion coefficients at point 1, before the rise, and at point 2, after completion,

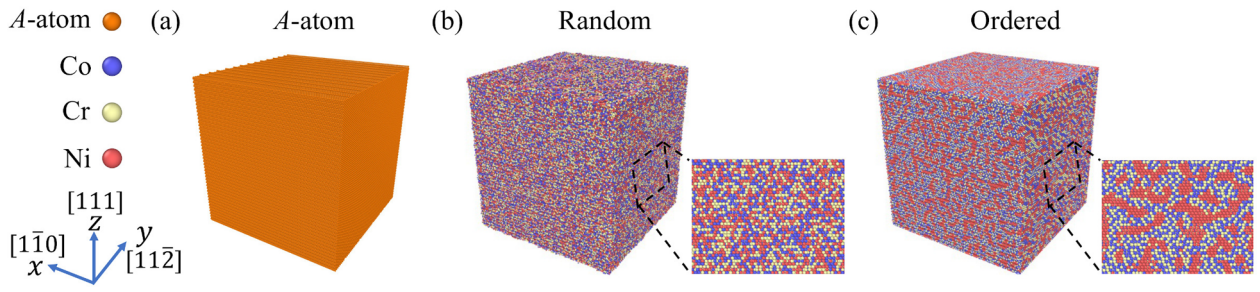

FIG. 1. Atomic configurations of the single crystalline (a) *A*-atom sample, (b) random, and (c) ordered CoCrNi MEAs. The *A*-atom is a mean-field model of the MEA produced by an *A*-atom potential, while the random and ordered MEAs represent the samples with an ideally random atomic distribution and with CSRO, respectively.

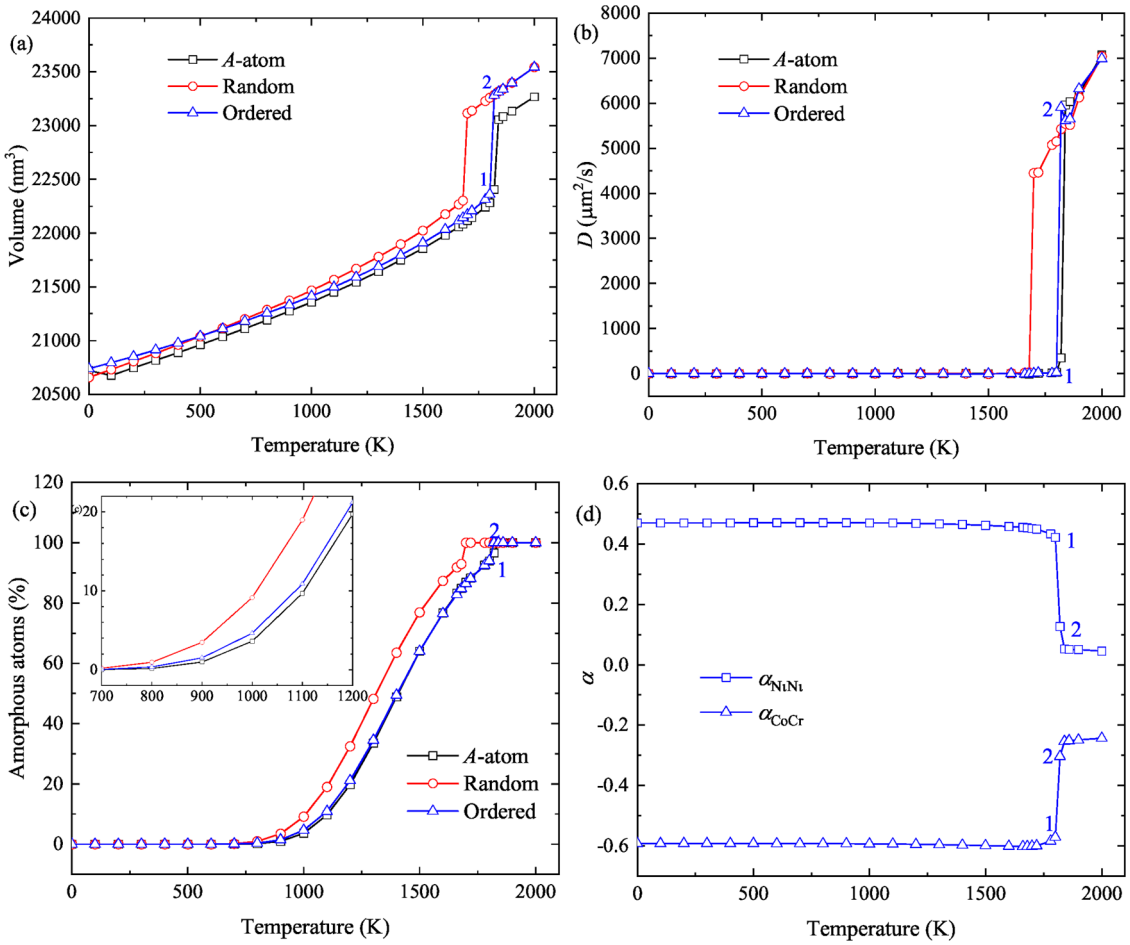

FIG. 2. (a) The volume, (b) diffusion coefficient D, and (c) percentage of amorphous atoms as a function of temperature during melting of the A-atom sample and the random and ordered CoCrNi MEAs. (d) The CSRO parameters α_{NiNi} and α_{CoCr} as the function of temperature for the ordered CoCrNi MEA. Points 1 and 2 are marked in the curves of the ordered MEA to denote the temperature range of 20 K, within which the melting temperature lies.

are comparable to those for solid and liquid Cu.[36,37] Therefore, the solid–liquid transition, i.e., melting, occurs between points 1 and 2. Here, we refer to the average temperature at points 1 and 2 as the melting temperature with ±10 K error. Results show that the melting temperature is 1830 K, the highest for the A-atom sample; 1810 K for the ordered MEA; and 1690 K, the lowest for the random MEA. These melting temperatures are close to 1690 K, the experimental melting temperature for polycrystalline CoCrNi MEA, determined by heating the sample from room temperature.[38] To some extent, the incremental heating in our calculation causes superheating, which has also been reported in experiments when the temperature rise is steep.[39] Due to superheating, the melting temperature exceeds the equilibrium melting temperature calculated by the solid–liquid coexistence method.[21,40] For comparison, the equilibrium melting temperatures of random MEA, ordered MEA, and A-atom sample are 1412, 1475, and 1543 K, respectively. The rank order is the same as that calculated in incremental heating. Incremental heating is selected for the calculations to follow since it is more appropriate for studying the physical process underlying melting. Figure S5 in the supplementary material also shows the melting temperature as a function of LD parameter FWHM or CSRO parameters α_{ij} (α_{NiNi} and α_{CoCr}) during the incremental heating. The melting temperature increases with the decrease in FWHM and the increase in the absolute values of α_{NiNi} and α_{CoCr}. This suggests that lower degree of LD and higher degree of CSRO lead to higher melting temperature. In addition, we carry out simulations with various sizes and initial random atomic distribution, as shown in Figs. S2 and S3, respectively. Results show that simulation cells used in this work are large enough to achieve convergence in the melting temperature, and the different random atomic distributions produce very similar melting temperatures.

To examine the structural changes in melting, the formation and growth of amorphization are studied as temperature rises. Figure 2(c) compares the percent of the amorphous atoms as the function of temperature among the three samples. Amorphous atoms refer to those atoms whose coordination with nearest neighbor atoms deviates from any kind of periodic arrangement. Below 800 K, the numbers of the amorphous atoms in all three samples are not more than 1%. When the temperature exceeds 800 K, the number of amorphous atoms in

the random MEA increases rapidly to 93% at 1680 K, point 1. Then, from point 1 to point 2, over the solid–liquid transition, it finally rises to 100%. Thus, all atoms become amorphous when solid–liquid transition, namely, melting, is completed. Another implication is that the solid at a high temperature can still contain large amounts of amorphous atoms ($\geq$ 90%). Compared to the random MEA, the amorphous atoms increase rapidly at a slightly higher temperature (900 K) in the *A*-atom sample, suggesting that LD in the random MEA can lower the energy barrier for forming amorphous atoms and significantly lower the temperature to initiate it. In addition, the temperature for the rapid proliferation of the amorphous atoms in the ordered MEA is also 100 K higher than that of the random MEA, implying that CSRO leads to a higher energy barrier for the nucleation of amorphization and the ordered MEA has a better thermal stability.

To observe how melting affects CSRO, Fig. 2(d) shows the CSRO parameter-temperature curves of the ordered MEA. Both α_{NiNi} and α_{CoCr} are found not to vary dramatically until point 1. From points 1 to 2, α_{NiNi} reduces from 0.422 to 0.127, while the absolute value of α_{CoCr} from 0.571 to 0.303. The substantial reductions in these two parameters indicate diminishing degrees of CSRO. Considering both these two parameters and the percent of the amorphous atoms in the ordered MEA [Fig. 2(c)] indicates that the CoCr clusters and Ni segregated regions in the ordered MEA are not fully removed, even at the high temperature of 1800 K, i.e., point 1, when most atoms within them do not belong to an FCC lattice structure but to amorphous clusters. Only when the melting is completed at point 2, the CSRO regions have been eliminated and all three types of atoms in the ordered MEA become distributed randomly in the melting liquid.

To understand the influence of LD and CSRO on the initiation of melting, the atomic configurations of all three samples at the start of melting, which is 1000 K, are studied. As shown in Figs. 3(a) and 3(b), the amorphous clusters are distributed uniformly in the *A*-atom and random MEA samples, indicating homogeneous nucleation. It further suggests that LD in the random MEA does not provide preferential nucleation sites, since LD exists everywhere. Compared to the *A*-atom sample at 1000 K, the random MEA has a higher density of amorphous clusters, further confirming that LD in random MEA remarkably lowers the energy barrier for the amorphization nucleation. In contrast, study of the ordered MEA in Fig. 3(c) reveals that the CoCr regions and the boundaries between the CoCr clusters and surrounding Ni-rich regions are preferred sites for amorphous clusters formation. More specifically, it is the LD within CoCr regions and at the boundaries of CSRO regions that promotes the nucleation of the amorphous cluster. Compared to random MEA, the ordered MEA has a smaller area for the preferred nucleation of amorphous clusters and, thus, fewer amorphous clusters at the moment of the initial melting, e.g., at 1000 K. Since lattice instability, amorphization, and melting may be related to the local stress,[41–43] we show the distribution of volumetric stress $(\sigma_{xx} + \sigma_{yy} + \sigma_{zz})/3$ at 0 K in Fig. S4 of the supplementary material. In general, the volumetric stress level is the highest and the stress fluctuation is the most significant in the random MEA, followed by the ordered MEA and the *A*-atom sample. Thus, the higher volumetric stress induced by LD can promote lattice instability, amorphization and melting, causing a lower melting temperature.

For all samples, in Fig. 4, we present the atomic configurations and the corresponding XRD patterns at four representative temperatures during the melting process. This comparison helps to build a one-to-one mapping between the structural evolution in real space and the diffraction information in reciprocal space.[27,44] All three samples are solids with ideal FCC lattice structures and no amorphous atoms at 0 K. Their diffraction patterns, however, show some differences. For the *A*-atom sample, six {110} spots regularly spaced around the (000) spot, while for the random MEA, these same spots have broadened and are weaker in intensity. The comparison suggests that this change is a likely consequence of the LD present in the random MEA but absent in the *A*-atom sample. In addition, we observe many small spots scattered around the central spot, again a result of the LD, distributed over the sample. Similarly, a comparison between the random MEA and ordered MEA samples reveals some distinctly different diffraction spots, i.e., 1/3{121} spots, appearing in the x-ray pattern of the ordered MEA. More interestingly, the x-ray pattern of the ordered MEA is much cleaner than that of the random MEA. Most of the spots

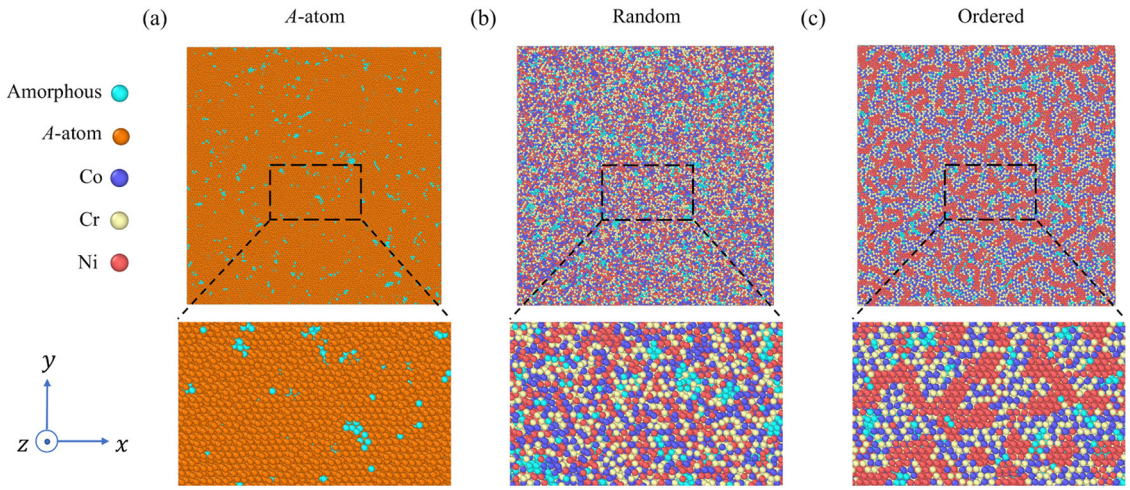

FIG. 3. Atomic configurations of the (a) *A*-atom sample, (b) random, and (c) ordered CoCrNi MEAs at 1000 K. The amorphous atoms are colored in cyan.

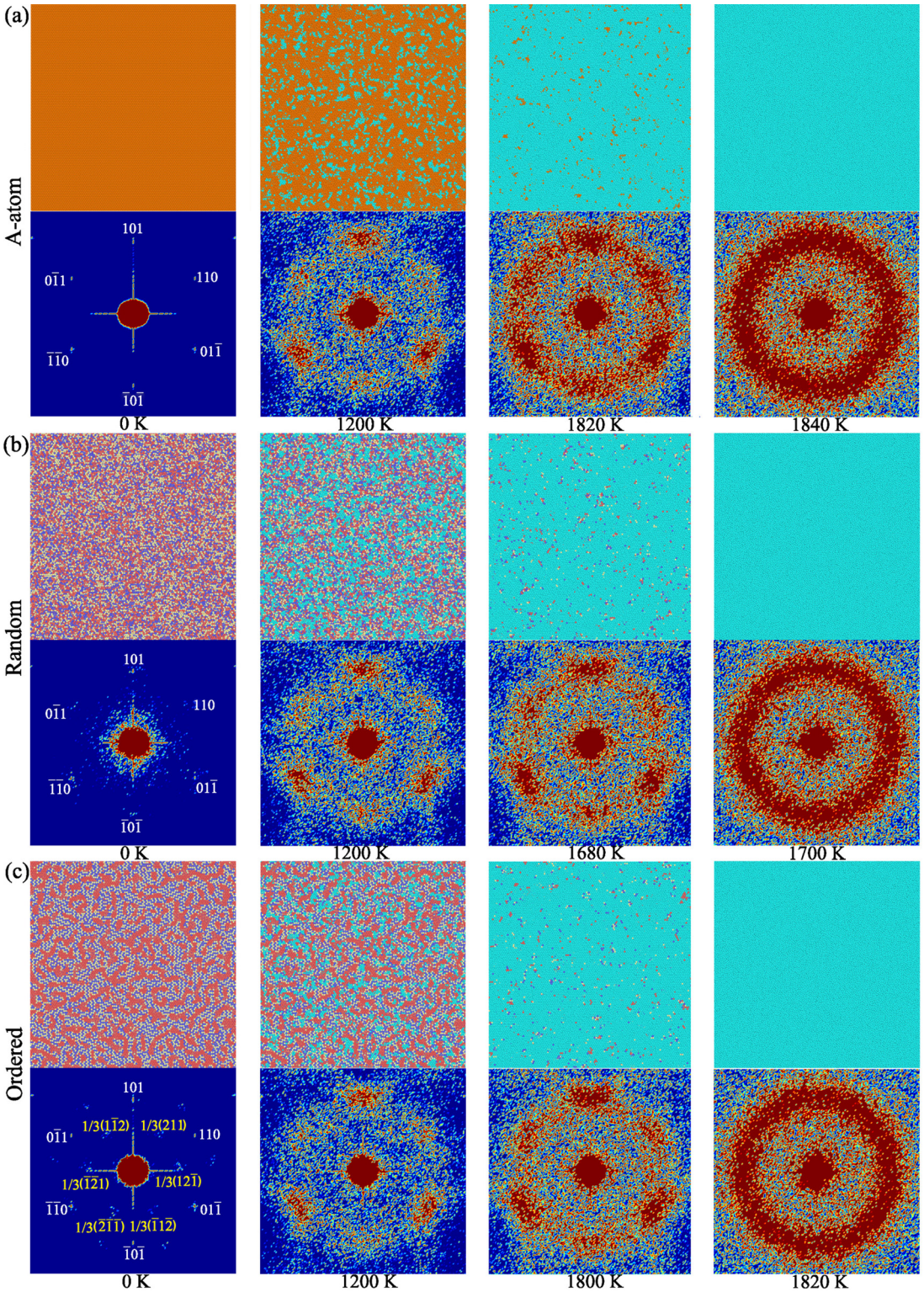

FIG. 4. Atomic configurations and corresponding XRD patterns of the (a) *A*-atom sample, (b) random, and (c) ordered CoCrNi MEAs at different temperatures. The atoms are colored in the same way as in Figs. 1 and 3.

scattered around the central spot in the random MEA are absent in the ordered MEA. These differences are signatures of the CSRO, likely resulting from the localization of the LD to the CoCr regions and the interfaces between the Ni regions and CoCr clusters. Thus, LD and CSRO in real space can be reflected by the diffraction spots in reciprocal space.

As the temperature increases in all three samples, the lattice is perturbed by thermal fluctuations and amorphous atoms are generated. At the same time, due to greater lattice disorder, {101} diffraction spots become diffused and broadened and rotate along the Debyer–Scherrer ring and more small scattered spots appear. For the ordered MEA, the temperature rise additionally prompts the disappearance of the 1/3{121} spots and thus the decomposition of CSRO. As the temperature further rises to point 1, more than 90% of the atoms in these samples belong to amorphous clusters, while the entire samples are still solid. Compared to the diffraction spots at 1200 K, those at the point 1 temperature are more diffuse. When the temperature is increased by 20 K to point 2, all three samples completely melt. Their diffraction patterns display a continuous diffuse ring, which is characteristic of a liquid in reciprocal space. The simulated diffraction patterns in our simulations can be compared to those in *in situ* XRD experiments. Such a comparison provides an essential link between the x-ray patterns and spatial information on LD, CSRO, or the inhomogeneous amorphization process.

In summary, large-scale MD and XRD simulations are performed to investigate the effects of LD and CSRO on the melting of CoCrNi MEAs. As the temperature rises, LD and CSRO play different roles in initiating melting by affecting the nucleation sites of amorphous clusters. Due to its perfect atomic structure, without LD and CSRO, the pure *A*-atom sample has the highest melting temperature. Compared to the *A*-atom sample, the random CoCrNi MEA has a much lower melting temperature. Abundant LD in the random MEA can significantly reduce the energy barrier for the homogenous nucleation of amorphous clusters, thereby promoting their formation. In comparison with the random MEA, CSRO in the ordered MEA localizes LD to CoCr regions and the boundaries between the CoCr clusters and Ni segregated regions, where the amorphous clusters tend to nucleate. During melting of the ordered MEA, the CSRO decreases only slightly up to 95% of the melting temperature, but beyond this threshold, the degree of CSRO sharply reduces and the CoCr clusters and Ni segregated regions completely decompose. Finally, this study points to the ability of CSRO in MPEAs to enhance thermal stability.

See the supplementary material for additional data and figures, as referred to in the main text.

The authors thank Dr. Saeed Zare Chavoshi for helpful discussions on the solid–liquid coexistence method. W.R.J. and I.J.B. would like to acknowledge support from the Office of Naval Research under Grant No. N000141712810. Use was made of computational facilities purchased with funds from the National Science Foundation (No. CNS-1725797) and administered by the Center for Scientific Computing (CSC). The CSC is supported by the California NanoSystems Institute and the Materials Research Science and Engineering Center (MRSEC; No. NSF DMR 1720256) at UC Santa Barbara.

DATA AVAILABILITY

The data that support the findings of this study are available within the article and its supplementary material.

REFERENCES

[1]H. Diao, R. Feng, K. A. Dahmen, and P. Liaw, "Fundamental deformation behavior in high-entropy alloys: An overview," Curr. Opin. Solid State Mater. Sci. **21**, 252–266 (2017).
[2]Y. Ye, Q. Wang, J. Lu, C. Liu, and Y. Yang, "High-entropy alloy: Challenges and prospects," Mater. Today **19**, 349–362 (2016).
[3]Y. Zhang, T. T. Zuo, Z. Tang, M. C. Gao, K. A. Dahmen, P. K. Liaw, and Z. P. Lu, "Microstructures and properties of high-entropy alloys," Prog. Mater. Sci. **61**, 1–93 (2014).
[4]E. Pickering and N. Jones, "High-entropy alloys: A critical assessment of their founding principles and future prospects," Int. Mater. Rev. **61**, 183–202 (2016).
[5]Z. Li, S. Zhao, R. O. Ritchie, and M. A. Meyers, "Mechanical properties of high-entropy alloys with emphasis on face-centered cubic alloys," Prog. Mater. Sci. **102**, 296–345 (2019).
[6]S. Chen, Y. Tong, and P. K. Liaw, "Additive manufacturing of high-entropy alloys: A review," Entropy **20**, 937 (2018).
[7]J. M. Torralba and M. Campos, "High entropy alloys manufactured by additive manufacturing," Metals **10**, 639 (2020).
[8]A. O. Moghaddam, N. A. Shaburova, M. N. Samodurova, A. Abdollahzadeh, and E. A. Trofimov, "Additive manufacturing of high entropy alloys: A practical review," J. Mater. Sci. Technol. **77**, 131–162 (2020).
[9]P. Niu, R. Li, K. Gan, T. Yuan, S. Xie, and C. Chen, "Microstructure, properties, and metallurgical defects of an equimolar CoCrNi medium entropy alloy additively manufactured by selective laser melting," Metall. Mater. Trans. A **52**, 753–766 (2021).
[10]S. Xu, E. Hwang, W.-R. Jian, Y. Su, and I. J. Beyerlein, "Atomistic calculations of the generalized stacking fault energies in two refractory multi-principal element alloys," Intermetallics **124**, 106844 (2020).
[11]S. Xu, Y. Su, W.-R. Jian, and I. J. Beyerlein, "Local slip resistances in equal-molar MoNbTi multi-principal element alloy," Acta Mater. **202**, 68–79 (2021).
[12]H. S. Oh, D. Ma, G. P. Leyson, B. Grabowski, E. S. Park, F. Körmann, and D. Raabe, "Lattice distortions in the FeCoNiCrMn high entropy alloy studied by theory and experiment," Entropy **18**, 321 (2016).
[13]Y. Zhao, Z. Lei, Z. Lu, J. Huang, and T. Nieh, "A simplified model connecting lattice distortion with friction stress of Nb-based equiatomic high-entropy alloys," Mater. Res. Lett. **7**, 340–346 (2019).
[14]F. Otto, A. Dlouhý, K. G. Pradeep, M. Kuběnová, D. Raabe, G. Eggeler, and E. P. George, "Decomposition of the single-phase high-entropy alloy CrMnFeCoNi after prolonged anneals at intermediate temperatures," Acta Mater. **112**, 40–52 (2016).
[15]R. Zhang, S. Zhao, J. Ding, Y. Chong, T. Jia, C. Ophus, M. Asta, R. O. Ritchie, and A. M. Minor, "Short-range order and its impact on the CrCoNi medium-entropy alloy," Nature **581**, 283–287 (2020).
[16]X. Chen, Q. Wang, Z. Cheng, M. Zhu, H. Zhou, P. Jiang, L. Zhou, Q. Xue, F. Yuan, J. Zhu, W. Xiaolei, and E. Ma, "Direct observation of chemical short-range order in a medium-entropy alloy," Nature **592**, 712–716 (2021).
[17]Y. Zhao and T. Nieh, "Correlation between lattice distortion and friction stress in Ni-based equiatomic alloys," Intermetallics **86**, 45–50 (2017).
[18]Q.-J. Li, H. Sheng, and E. Ma, "Strengthening in multi-principal element alloys with local-chemical-order roughened dislocation pathways," Nat. Commun. **10**, 3563 (2019).
[19]W.-R. Jian, Z. Xie, S. Xu, Y. Su, X. Yao, and I. J. Beyerlein, "Effects of lattice distortion and chemical short-range order on the mechanisms of deformation in medium entropy alloy CoCrNi," Acta Mater. **199**, 352–369 (2020).
[20]L. Zheng, Q. An, Y. Xie, Z. Sun, and S.-N. Luo, "Homogeneous nucleation and growth of melt in copper," J. Chem. Phys. **127**, 164503 (2007).
[21]S. Z. Chavoshi, S. Xu, and S. Goel, "Addressing the discrepancy of finding the equilibrium melting point of silicon using molecular dynamics simulations," Proc. R. Soc. A **473**, 20170084 (2017).
[22]L.-B. Han, Q. An, R.-S. Fu, L. Zheng, and S.-N. Luo, "Melting of defective Cu with stacking faults," J. Chem. Phys. **130**, 024508 (2009).

[23]L. Wang, X. Zhang, L. Deng, J. Tang, S. Xiao, H. Deng, and W. Hu, "Surface premelting/recrystallization governing the collapse of open-cell nanoporous Cu via thermal annealing," Phys. Chem. Chem. Phys. **20**, 16184–16192 (2018).
[24]P. Bavli, E. Polturak, and J. Adler, "Molecular dynamics study of melting of the hcp metal Mg," Phys. Rev. B **84**, 235442 (2011).
[25]V. Sorkin, E. Polturak, and J. Adler, "Molecular dynamics study of melting of the bcc metal vanadium. II. Thermodynamic melting," Phys. Rev. B **68**, 174103 (2003).
[26]C. Tymczak and J. R. Ray, "Asymmetric crystallization and melting kinetics in sodium: A molecular-dynamics study," Phys. Rev. Lett. **64**, 1278 (1990).
[27]L. Wang, J. E, Y. Cai, F. Zhao, D. Fan, and S. Luo, "Shock-induced deformation of nanocrystalline Al: Characterization with orientation mapping and selected area electron diffraction," J. Appl. Phys. **117**, 084301 (2015).
[28]W. Jian, X. Yao, L. Wang, X. Tang, and S. Luo, "Short- and medium-range orders in $Cu_{46}Zr_{54}$ metallic glasses under shock compression," J. Appl. Phys. **118**, 015901 (2015).
[29]L. Wang, Y. Cai, A.-M. He, and S. Luo, "Second yield via dislocation-induced premelting in copper," Phys. Rev. B **93**, 174106 (2016).
[30]S. Plimpton, "Fast parallel algorithms for short-range molecular dynamics," J. Comp. Phys. **117**, 1–19 (1995).
[31]J. Cowley, "An approximate theory of order in alloys," Phys. Rev. **77**, 669 (1950).
[32]D. de Fontaine, "The number of independent pair-correlation functions in multicomponent systems," J. Appl. Crystall. **4**, 15–19 (1971).
[33]P. M. Larsen, S. Schmidt, and J. Schiøtz, "Robust structural identification via polyhedral template matching," Modell. Simul. Mater. Sci. Eng. **24**, 055007 (2016).
[34]A. Stukowski, "Visualization and analysis of atomistic simulation data with OVITO—The Open Visualization Tool," Modell. Simul. Mater. Sci. Eng. **18**, 015012 (2010).
[35]V. Sorkin, E. Polturak, and J. Adler, "Molecular dynamics study of melting of the bcc metal vanadium. I. Mechanical melting," Phys. Rev. B **68**, 174102 (2003).
[36]F. Zhao, B. Li, W. Jian, L. Wang, and S. Luo, "Shock-induced melting of honeycomb-shaped Cu nanofoams: Effects of porosity," J. Appl. Phys. **118**, 035904 (2015).
[37]A. He, S. Duan, J.-L. Shao, P. Wang, and C. Qin, "Shock melting of single crystal copper with a nanovoid: Molecular dynamics simulations," J. Appl. Phys. **112**, 074116 (2012).
[38]Z. Wu, H. Bei, G. M. Pharr, and E. P. George, "Temperature dependence of the mechanical properties of equiatomic solid solution alloys with face-centered cubic crystal structures," Acta Mater. **81**, 428–441 (2014).
[39]Q. Mei and K. Lu, "Melting and superheating of crystalline solids: From bulk to nanocrystals," Prog. Mater. Sci. **52**, 1175–1262 (2007).
[40]J. R. Morris, C. Wang, K. Ho, and C. Chan, "Melting line of aluminum from simulations of coexisting phases," Phys. Rev. B **49**, 3109 (1994).
[41]V. I. Levitas, H. Chen, and L. Xiong, "Lattice instability during phase transformations under multiaxial stress: Modified transformation work criterion," Phys. Rev. B **96**, 054118 (2017).
[42]H. Chen, V. I. Levitas, and L. Xiong, "Amorphization induced by 60 shuffle dislocation pileup against different grain boundaries in silicon bicrystal under shear," Acta Mater. **179**, 287–295 (2019).
[43]T. Phan, J. Rigelesaiyin, Y. Chen, A. Bastawros, and L. Xiong, "Metallic glass instability induced by the continuous dislocation absorption at an amorphous/crystalline interface," Acta Mater. **189**, 10–24 (2020).
[44]S. Z. Chavoshi, S. Xu, and X. Luo, "Dislocation-mediated plasticity in silicon during nanometric cutting: A molecular dynamics simulation study," Mater. Sci. Semicond. Process. **51**, 60–70 (2016).